June 2006

Infrared optical properties of $Mg_{x-1}Zn_{1-x}O$ thin films ($0 \leq x \leq 1$): Long-wavelength optical phonons and dielectric constants

C. Bundemann
Institut für Experimentelle Physik II, Universität Leipzig, Linnéstrasse 5, D-04103 Leipzig, Germany

A. Rahm
Institut für Experimentelle Physik II, Universität Leipzig, Linnéstrasse 5, D-04103 Leipzig, Germany

M. Lorenz
Institut für Experimentelle Physik II, Universität Leipzig, Linnéstrasse 5, D-04103 Leipzig, Germany

M. Grundmann
Institut für Experimentelle Physik II, Universität Leipzig, Linnéstrasse 5, D-04103 Leipzig, Germany

Mathias Schubert
University of Nebraska - Lincoln, mschubert4@unl.edu

Infrared optical properties of $Mg_xZn_{1-x}O$ thin films ($0 \leqslant x \leqslant 1$): Long-wavelength optical phonons and dielectric constants

C. Bundesmann,[a] A. Rahm, M. Lorenz, and M. Grundmann
Institut für Experimentelle Physik II, Universität Leipzig, Linnéstrasse 5, D-04103 Leipzig, Germany

M. Schubert[b]
Department of Electrical Engineering, University of Nebraska-Lincoln, Lincoln, Nebraska 68588-0511, Center for Materials Research and Analysis, University of Nebraska-Lincoln, Lincoln, Nebraska 68588-0511, and Institut für Experimentelle Physik II, Universität Leipzig, Linnéstrasse 5, D-04103 Leipzig, Germany

(Received 1 February 2006; accepted 4 April 2006; published online 1 June 2006)

Infrared spectroscopic ellipsometry in the spectral range from $\omega=360$ cm^{-1} to $\omega=1500$ cm^{-1} and Raman scattering spectroscopy are applied to study the long-wavelength optical phonon modes and dielectric constants of $Mg_xZn_{1-x}O$ thin films in the composition range $0 \leqslant x \leqslant 1$. The samples were grown by pulsed laser deposition on sapphire substrates. X-ray diffraction measurements of the thin film samples reveal the hexagonal wurtzite crystal structure for $x \leqslant 0.53$ and the cubic rocksalt crystal structure for $x \geqslant 0.67$. A systematic variation of the phonon mode frequencies with Mg-mole fraction x is found for both hexagonal and cubic $Mg_xZn_{1-x}O$ thin films. The modified random isodisplacement model matches the observed composition dependence of the phonon mode frequencies for the hexagonal structure thin films [J. Chen and W. Z. Shen, Appl. Phys. Lett. **83**, 2154 (2003)], whereas a simple linear approximation scheme is sufficient for the cubic structure part. We observe a discontinuous behavior of the transverse optical phonon modes (decrease), and the static and high-frequency dielectric constants (increase) within the phase transition composition region from the wurtzite structure part to the rocksalt structure part. On the contrary, the longitudinal phonon mode parameters increase almost linearly, and upon phase transition the splitting between the transverse and longitudinal modes increases. We associate this discontinuous behavior with the change of the nearest-neighbor coordination number from fourfold (wurtzite structure) to sixfold (rocksalt structure) in our samples and the associated increase in bond ionicity from ZnO to MgO. Accordingly, we propose that the reduced exciton mass parameter should approximately double upon changing from wurtzite to rocksalt crystal structure. © *2006 American Institute of Physics*. [DOI: 10.1063/1.2200447]

I. INTRODUCTION

ZnO (wurtzite structure, hexagonal) and MgO (rocksalt structure, cubic) are wide-band-gap semiconducting materials with direct band-gap energies $E_g \sim 3.37$ eV (Ref. 1) and $E_g \sim 7.6$ eV,[2] respectively. Upon alloying of ZnO and MgO, where a phase transition must be obeyed, the direct band gap can be tuned into extremely short wavelength regions.[3–6] Therefore, the ternary alloy $Mg_xZn_{1-x}O$ is a promising candidate for future applications in optics and optoelectronics in the UV spectral region (light emitting diodes, laser diodes, or detectors).[7] Eventually, $Mg_xZn_{1-x}O$-based devices may compete with group-III–nitride-based optoelectronic devices.[3] Therefore, $Mg_xZn_{1-x}O$ continues to attract attention. In this report we summarize on the infrared optical properties and discuss their discontinuous behavior across the phase transition region.

Fundamental parameters for the design of optoelectronic devices with multiple layers are lattice and free charge carrier properties of the individual layers, such as crystal quality, strain, free charge carrier effective mass parameters, their anisotropy, and optical mobility parameters. Determination of the free charge carrier and phonon mode parameters of thin films in complex layered structures can be done by infrared spectroscopic ellipsometry (IRSE), which was demonstrated recently as an excellent technique for the precise measurement of the complex IR dielectric function (DF) of group III-V alloys in layered structures.[8–12] At IR wavelengths the DF is affected by polar phonon modes, free charge carrier excitations, and the background dielectric constant ε_∞ due to the high-frequency electronic transitions. For materials with a wurtzite structure, the DF differs for the electric field polarization parallel ($\varepsilon_\parallel$) and perpendicular ($\varepsilon_\perp$) to the c axis. A prerequisite for the determination of the free charge carrier parameters from DF analysis is the accurate knowledge of the phonon mode and ε_∞ contributions. Single crystalline $Mg_xZn_{1-x}O$ thin films with a sufficiently low number of free charge carriers are required for the measurement of these contributions to the DF. We have grown such films with the density of free charge carriers $n \leqslant 10^{17}$ cm^{-3} by pulsed laser deposition (PLD) on c-plane and r-plane sap-

[a]Present address: Leibniz-Institut für Oberflächenmodifizierung e.V., Permoserstraße 15, D-04303 Leipzig, Germany; electronic mail: carsten.bundesmann@iom-leipzig.de; URL: http://www.uni-leipzig.de/ellipsometrie
[b]Electronic mail: schubert@engr.unl.edu; URL: http://ellipsometry.unl.edu/

phire substrates. The focus of the present work is a comprehensive study of the phonon modes and dielectric constants of hexagonal and cubic $Mg_xZn_{1-x}O$ thin films. Our results are obtained from IRSE analysis in combination with Raman scattering measurements. The phonon mode parameter results obtained by both techniques are highly consistent with each other. The data presented here will enable future IRSE characterization of free charge carrier properties in doped $Mg_xZn_{1-x}O$-based heterostructures for optoelectronic device applications. We have recently reported IRSE measurements of IR DF spectra and phonon modes of ZnO.[13,14] Some of the results concerning the $Mg_xZn_{1-x}O$ thin films presented here were published in Refs. 6 and 15–17. This work summarizes the previously published data, experimental results of this group, and literature data from other groups.[18] In particular, we discuss the observed discontinuous behavior across the phase transition of the $Mg_xZn_{1-x}O$ thin films.

II. THEORY

A. Crystal structure

ZnO crystallizes in the wurtzite structure, which belongs to the hexagonal system with space group C_{6v}^4 ($P6_3mc$) in the Schoenflies (short standard) notation. Two atom species each occupy the positions of a closest packed hexagonal lattice. The two sublattices are shifted along the c axis against each other. In contrast to that, MgO crystallizes in the rocksalt structure, which belongs to the cubic system with space group O_h^1 ($Pm3m$). It consists of two face-centered cubic (fcc) sublattices, which are occupied by one atom species each. The two sublattices are shifted along one-half of the diagonal of the primitive unit cell against each other. Consequently, the ternary alloy $Mg_xZn_{1-x}O$ will exhibit a phase transition for some x.

It is known that the hexagonal ZnO and $Mg_xZn_{1-x}O$ thin films grown on c-plane and a-plane sapphires adopt a c-plane orientation, while those grown on r-plane sapphire adopt an a-plane orientation.[14,19–22]

B. Phonon modes

The primitive unit cell of a crystal with a wurtzite crystal structure contains four atoms, two of each atom species. Consequently, 12 phonon branches exist, three acoustical and nine-optical. The optical phonons at the Γ point of the Brillouin zone belong to the following irreducible representation:[23]

$$\Gamma^{\mathrm{opt}} = 1A_1 + 2B_1 + 1E_1 + 2E_2. \tag{1}$$

Hereby the branches with E_1 and E_2 symmetries are twofold degenerated. Both A_1 and E_1 modes are polar, and split into transverse (TO) and longitudinal optical (LO) phonons with different frequencies ω_{TO} and ω_{LO}, respectively, due to the macroscopic electric fields associated with the LO phonons. The short-range interatomic forces cause anisotropy. Therefore, A_1 and E_1 modes possess different frequencies. When the electrostatic forces dominate the anisotropy in the short-range forces, like in wurtzite ZnO, the TO-LO splitting is larger than the A_1-E_1 splitting. For the lattice vibrations with A_1 and E_1 symmetries, the atoms move parallel and perpendicular to the c axis, respectively. Both A_1 and E_1 modes are Raman and infrared active. The two nonpolar E_2 modes [$E_2^{(1)}$, $E_2^{(2)}$] are Raman active only. The B_1 modes are infrared and Raman inactive ("silent modes").

The Γ-point optical phonons of a crystal with a rocksalt crystal structure belong to the following irreducible representation:

$$\Gamma^{\mathrm{opt}} = F_{1u}. \tag{2}$$

The F_{1u} mode is polar, and splits into TO and LO modes. The F_{1u} mode is infrared active and Raman inactive.[24]

C. Infrared dielectric function

In the IR spectral region the DF is sensitive to phonon (lattice) and plasmon (free charge carrier) contributions. If the concentration of free charge carriers is small, only phonon mode contributions have to be considered. A common way to describe the contribution of l polar lattice modes is the following factorized form with Lorentzian broadening:

$$\varepsilon_j = \varepsilon_{\infty,j} \prod_{i-1}^{l} \frac{\omega_{\mathrm{LO},ij}^2 - \omega^2 - i\gamma_{\mathrm{LO},ij}\omega}{\omega_{\mathrm{TO},ij}^2 - \omega^2 - i\gamma_{\mathrm{TO},ij}\omega}. \tag{3}$$

The polar lattice modes split into TO ($\omega_{\mathrm{TO},ij}$) and LO modes ($\omega_{\mathrm{LO},ij}$), with broadening parameters $\gamma_{\mathrm{TO},ij}$ and $\gamma_{\mathrm{LO},ij}$, respectively.[8] The parameters $\varepsilon_{\infty,j}$ denote the high-frequency model dielectric function limits. The subscript j refers to the two polarization states parallel ($j=\parallel$) and perpendicular ($j=\perp$) to the c axis, which have to be distinguished in optically uniaxial samples. Modes addressed by the DF for polarization $E\parallel c$ or $E\perp c$ correspond to phonons with A_1 or E_1 symmetry, respectively.

The high-frequency dielectric constants $\varepsilon_{\infty,j}$ are related to the static dielectric constants $\varepsilon_{0,j}$ by the Lydanne-Sachs-Teller relation[25]

$$\varepsilon_{0,j} = \varepsilon_{\infty,j} \prod_{i=1}^{l} \frac{\omega_{\mathrm{LO},i}^2}{\omega_{\mathrm{TO},i}^2}. \tag{4}$$

In some cases ε_j must also account for IR-active modes with small LO-TO splitting $d\omega_\nu^2 = \omega_{\mathrm{LO},\nu}^2 - \omega_{\mathrm{TO},\nu}^2$ ($\nu = 1, \ldots, n$) and broadening parameters $\delta\gamma_\nu = \gamma_{\mathrm{LO},\nu} - \gamma_{\mathrm{TO},\nu}$.[26] Modes with low polarity, such as impurity modes (IMs, $\omega_{\mathrm{LO},\nu} \equiv \omega_{\mathrm{TO},\nu}$), contribute to ε_j as a small perturbation only. Lattice imperfections may cause vibrational modes confined to respective lattice sites, and with frequencies, which commonly differ from the host lattice modes. Alloying disorder can also induce subtle modes of small polarity, supposedly caused by different states of local atomic order and/or composition roughness, which can be well described by the "impurity mode" model.[27] In the case of l polar lattice and n impurity modes, ε_j reads

$$\varepsilon_j = \varepsilon_{\infty,j} \prod_{i-1}^{l} \frac{\omega_{\mathrm{LO},ij}^2 - \omega^2 - i\gamma_{\mathrm{LO},ij}\omega}{\omega_{\mathrm{TO},ij}^2 - \omega^2 - i\gamma_{\mathrm{TO},ij}\omega} \times \prod_{\nu=1}^{n} \left(1 + \frac{i\delta\gamma_{\nu j} - \delta\omega_{\nu j}^2}{\omega^2 + i\gamma_{\mathrm{IM},\nu j}\omega - \omega_{\mathrm{IM},\nu j}} \right). \tag{5}$$

D. Ellipsometry

Ellipsometry determines the change of polarization state upon reflection (or transmission).[28,29] Two different approaches, standard and generalized ellipsometries, have to be distinguished. Standard ellipsometry is applied when no light polarized perpendicular (s) to the plane of incidence is converted into light polarized parallel (p) to the plane of incidence, or vice versa. This is the case for optically isotropic samples or optically uniaxial samples, where the optical axis (c axis) is perpendicular to the sample surface. In all other cases the generalized ellipsometry approach has to be applied.

Applying the Jones matrix formalism, generalized ellipsometry determines three ratios of reflection coefficients for polarized light out of the four complex-valued elements of the Jones reflection matrix $\mathbf{r}$, which relates the incident (A_i) and reflected plane waves (B_i) as follows:[8]

$$\begin{pmatrix} B_p \\ B_s \end{pmatrix} = \mathbf{r} \begin{pmatrix} A_p \\ A_s \end{pmatrix} = \begin{pmatrix} r_{pp} & r_{sp} \\ r_{ps} & r_{ss} \end{pmatrix} \cdot \begin{pmatrix} A_p \\ A_s \end{pmatrix}. \tag{6}$$

Here the first subscript of the reflection matrix elements r_{ij} denotes the incident polarization and the second subscript denotes the outgoing polarization. The generalized ellipsometry parameters Ψ_{ij} and Δ_{ij}, which are measured within the experiment, are defined as follows:

$$\frac{r_{pp}}{r_{ss}} \equiv R_{pp} = \tan \Psi_{pp} \exp(i\Delta_{pp}), \tag{7}$$

$$\frac{r_{ps}}{r_{pp}} \equiv R_{ps} = \tan \Psi_{ps} \exp(i\Delta_{ps}), \tag{8}$$

$$\frac{r_{sp}}{r_{ss}} \equiv R_{sp} = \tan \Psi_{sp} \exp(i\Delta_{sp}). \tag{9}$$

Further details about generalized ellipsometry are given in Refs. 8, 28, and 30.

When the off-axis elements of the Jones reflection matrix are zero, standard ellipsometry is applied and only one ratio ρ of reflection coefficients is determined

$$\rho = \left(\frac{B_p}{B_s}\right) \Big/ \left(\frac{A_p}{A_s}\right) = r_{pp}/r_{ss} = \tan \Psi \exp(i\Delta). \tag{10}$$

In general, the measured ellipsometry parameters depend on the photon energy $\hbar\omega$, the layer sequence within the sample, each layer's DF, each layer's thickness d, the DFs of the substrate material and of the ambient material, and the angle of incidence Φ_a.[28] In the case of nonisotropic samples, the crystal orientation must be considered too. The crystal orientation can be described by Euler angles. For uniaxial films two (θ and φ) out of three Euler angles are sufficient. Thereby θ denotes the angle between the c axis and the sample normal (out-of-plane tilt), and φ denotes the angle between the projection of the c axis onto the sample surface and the plane of incidence (in-plane azimuth).[8]

The experimental data are analyzed by a point-by-point model analysis or a model line shape analysis. Traditionally, a point-by-point or wavelength-by-wavelength analysis is performed, where real and imaginary numbers of the dielectric functions of interest at each photon energy are varied independently of all other spectral data points until the thereby generated ellipsometry data match the experimental data as close as possible.

In order to perform a point-by-point analysis, in general, the thickness of the layer of interest and the dielectric functions and thicknesses of all other sample constituents must be known.[26] In the special case of off-axis oriented uniaxial samples, e.g., a-plane oriented hexagonal thin films, the generalized ellipsometry data contain sensitivity to the thickness d, the c-axis orientation, and the dielectric functions $\varepsilon_{\parallel}$ and $\varepsilon_{\perp}$ upon combined analysis of multiple measurements at different sample in-plane azimuths and angles of incidence, as have been recently demonstrated for an a-plane ZnO thin film on r-plane sapphire.[14]

A model line shape analysis is based on model dielectric functions [MDFs, see Eqs. (3) and (5)]. It is used to extract physically relevant parameters out of the dielectric functions obtained by a point-by-point analysis, or to study samples, where the conditions for a point-by-point analysis are not fulfilled, e.g., if the thickness is not known for all sample constituents. The point-by-point analysis is also not applicable for c-plane oriented uniaxial thin films, because the number of available independent parameters (Ψ and Δ for every photon energy regardless of the angle of incidence) is less than the number of experimental properties to be extracted (the complex dielectric functions $\varepsilon_{\parallel}$ and $\varepsilon_{\perp}$, and the layer thickness d).[8,13]

IRSE analysis of c-plane oriented, hexagonal $Mg_xZn_{1-x}O$ thin films does not provide sensitivity to the entire set of MDF parameters. For instance, the IRSE beam cannot sense the A_1(TO) mode. Its frequency must be taken from Raman scattering measurements as an input parameter for the IRSE analysis. This problem does not occur for a-plane oriented $Mg_xZn_{1-x}O$ thin films measured by generalized ellipsometry, as will be described below.

E. Local modes

Incorporation of additional atoms can cause vibrational modes, which are separated from the host lattice modes. If the number of impurity atoms is small compared to the number of host lattice atoms, the induced mode is "localized," i.e., its eigenvector does not have a sinusoidal or wavelike dependence on space, but is strongly peaked at the impurity atom, and falls off rapidly one or two lattice sites away.[31] These modes are called local modes. In Ref. 32 a simple model for the calculation of local modes in three-dimensional crystals was introduced. According to Ref. 32, the local modes of Mg in ZnO can be calculated by

$$\omega^2_{\mathrm{loc},1/2} = \frac{2\omega_1^2 + (1-\eta^2_{\mathrm{Zn}})\omega_2^2 \pm \sqrt{4\eta^2_{\mathrm{Zn}}\omega_1^4 + (1-\eta^2_{\mathrm{Zn}})^2\omega_2^4}}{2(1-\eta^2_{\mathrm{Zn}})} \tag{11}$$

if the Zn atom is substituted by the Mg atom, or by

TABLE I. Input parameters for the calculation of the local modes of Mg in ZnO (Table II).

Parameter		A_1 symmetry	E_1 symmetry
M_{Zn}, M_O, M_{Mg}	(amu)	65.4, 16.0, 24.3	
η_{Zn}, η_O		0.628, −0.519	
ω_{TO}, ω_{LO}	(cm^{-1})	378,575	409,590
ω_1, ω_2	(cm^{-1})	201,406	212,428

$$\omega^2_{\mathrm{loc},3/4} = \frac{2\omega_2^2 + (1-\eta_O^2)\omega_1^2 \pm \sqrt{4\eta_O^2\omega_2^4 + (1-\eta_O^2)^2\omega_1^4}}{2(1-\eta_O^2)} \tag{12}$$

if the O atom is replaced by the Mg atom. η_{Zn} and η_O are mass defect parameters given by

$$\eta_{Zn} = 1 - M_{Mg}/M_{Zn} \text{ and } \eta_O = 1 - M_{Mg}/M_O, \tag{13}$$

where M_{Zn}, M_O, and M_{Mg} are the atomic masses of Zn, O, and Mg, respectively. ω_1 and ω_2 are weighted frequency parameters defined by

$$\omega_1^2 = \frac{2\omega_{TO}^2 + \omega_{LO}^2}{3 + (3M_{Zn}/M_O)} \text{ and } \omega_2^2 = \frac{2\omega_{TO}^2 + \omega_{LO}^2}{3 + (3M_O/M_{Zn})}. \tag{14}$$

ω_{TO} and ω_{LO} are the TO- and LO-mode frequencies, respectively, of the host lattice ZnO. Table I summarizes the input parameters for the calculation of the local mode frequencies. Table II summarizes the calculated local mode frequencies of Mg in ZnO. In the case that the heaviest host lattice atom is substituted by an even heavier atom, no local mode is predicted.[32,33] Therefore, Zn should not introduce a local mode in MgO when Mg is substituted by Zn.

III. EXPERIMENT

$Mg_xZn_{1-x}O$ thin films are deposited by PLD on $10\times10\times0.5$ mm^3 sized *c*-plane sapphire (0001) and *r*-plane sapphire ($1\bar{1}02$) substrates.[34] A Lambda Physik LPX 305 KrF excimer laser, operating at $\lambda = 248$ nm, is used for target ablation. The polycrystalline ablation targets are prepared using a standard powder chemical route by ball milling ZnO (5 N) together with MgO (4 N) powder, cold pressing, and subsequent target sintering at $T = 1100$ °C for 12 h in air.

The crystal structure of the $Mg_xZn_{1-x}O$ thin films is investigated by x-ray diffraction (XRD). Rutherford backscattering spectrometry (RBS) is applied to determine the composition of the thin films.[35]

The IRSE spectra are recorded with a variable-polarizer, rotating-compensator-type spectroscopic ellipsometer at room temperature from $\omega = 360$ cm^{-1} to $\omega = 1500$ cm^{-1}, with a spectral resolution of 2 or 4 cm^{-1}, and typically at two angles of incidence between $\Phi_a = 50°$ and $\Phi_a = 70°$. IRSE spectra are analyzed with a three-phase model (ambient/thin film/substrate) and by application of a point-by-point or a model line shape analysis. In the later case, the DFs of the $Mg_xZn_{1-x}O$ are modeled according to Eqs. (3) and (5). The DFs of the sapphire substrate are taken from Ref. 36 as input parameters.

Raman scattering experiments are performed using a Dilor XY800 spectrometer with a spectral resolution of $\leqslant 4$ cm^{-1}. The 514.53 nm line of an Ar^+-ion laser is used for excitation and the incident laser power is $P \sim 50$ mW. The spectra are recorded in five backscattering configurations: $z(xy)z'$, $z(xx)z'$, $x(zy)x'$, $x(zz)x'$, and $x(yy)x'$. The notation follows the "Porto notation" introduced in Ref. 23. Hereby the *z* direction of the laboratory coordinate system is chosen parallel to the hexagonal *c* axis. The Raman spectra are analyzed with Lorentzian line shapes to determine the center frequencies of the Raman peaks. The estimated frequency error is less than half of the spectral resolution ($\leqslant 2$ cm^{-1}).

TABLE II. Local mode frequencies of Mg in ZnO calculated by Eqs. (11) and (12). All values are given in units of cm^{-1}.

Symmetry	Mg replaces Zn		Mg replaces O	
	$\omega_{loc,1}$	$\omega_{loc,2}$	$\omega_{loc,3}$	$\omega_{loc,4}$
E_1	518	251	636[a]	375
A_1	492	238	604[a]	357

[a]No local mode predicted (Refs. 32 and 33.

IV. RESULTS AND DISCUSSION

A. Crystal structure

In the ternary alloy $Mg_xZn_{1-x}O$ a phase transition from wurtzite (ZnO) to rocksalt (MgO) crystal structure occurs. It was reported that for PLD-grown $Mg_xZn_{1-x}O$ films MgO segregates from the hexagonal $Mg_xZn_{1-x}O$ for $x \geqslant 0.33$, which was explained to be due to the nonequilibrium nature of the PLD process.[3] In Ref. 37 the phase transition for PLD-grown $Mg_xZn_{1-x}O$ thin films was observed for $x > 0.45$. A similar value ($x \sim 0.47$) was found for $Mg_xZn_{1-x}O$ thin films grown by reactive electron beam evaporation (REBE).[18,38] A theoretical work predicts that heterostructural MgO-ZnO is stable in the rocksalt crystal structure for $x > 0.33$.[39] In contrast to that, the XRD results of the $Mg_xZn_{1-x}O$ thin film studied here reveal a hexagonal crystal structure for $x \leqslant 0.53$ and a cubic crystal structure for $x \geqslant 0.67$.

In Fig. 1 XRD 2Θ-ω scans of $Mg_xZn_{1-x}O$ thin films with $x = 0$, 0.15, 0.39, and 0.53 are plotted. The four dominant structures in the plots are assigned to the hexagonal (0 0 0 2) and (0 0 0 4) lattice reflections of the $Mg_xZn_{1-x}O$ thin films, and to the (0 0 0 6) and (0 0 0 1 2) lattice reflections of the sapphire substrate. For the $Mg_{0.53}Zn_{0.47}O$ thin film a further peak occurs at about $2\Theta = 78°$. This peak is assigned to the (2 2 2) lattice reflection peak of the cubic phase. However, its intensity is much lower than the intensity of the hexagonal lattice reflections. Our $Mg_xZn_{1-x}O$ thin films with $x \leqslant 0.53$ possess a hexagonal crystal structure with a minor cubic phase for $x = 0.53$.

Figure 2 depicts XRD 2Θ-ω scans of $Mg_xZn_{1-x}O$ thin films with $x = 0.69$, 0.88, and 1. The dominant peaks are assigned to the cubic (1 1 1) and (2 2 2) lattice reflections of the $Mg_xZn_{1-x}O$ thin films, and again to the (0 0 0 6) and (0 0 0 1 2) lattice reflections of the sapphire substrate. No hexagonal lattice reflection peaks can be seen, which indicates a single phase cubic structure for the $Mg_xZn_{1-x}O$ thin films with $x \geqslant 0.67$.

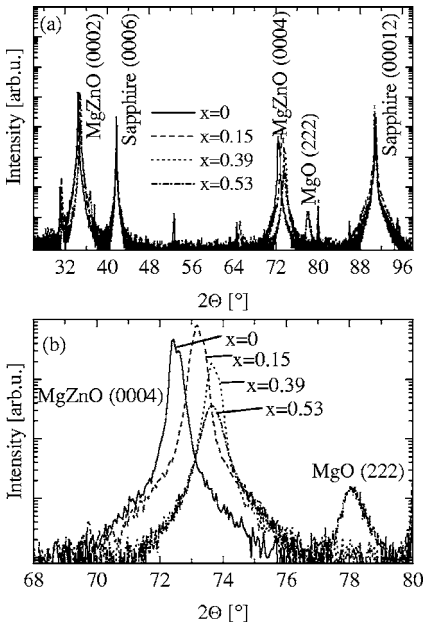

FIG. 1. (a) XRD 2Θ-ω scans of hexagonal $Mg_xZn_{1-x}O$ thin films with $x=0$, 0.15, 0.39, and 0.53. (b) Enlargement of the (0 0 0 4) reflection peak range. The duplet structure of the reflections is caused by the Cu $K\alpha_1$ and Cu $K\alpha_2$ lines of the x-ray diffractometer source.

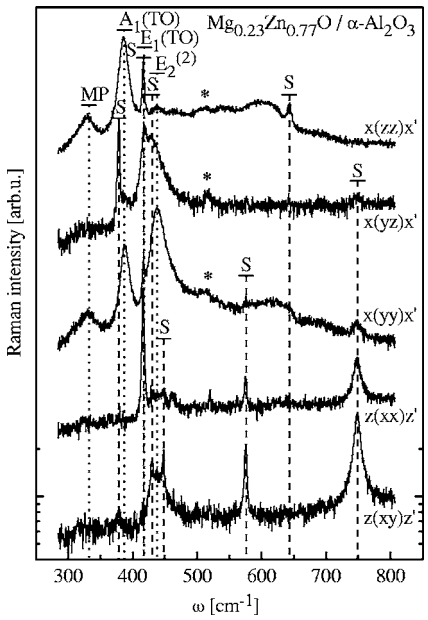

FIG. 3. Polarized micro-Raman spectra of a $Mg_{0.23}Zn_{0.77}O$ thin film on *c*-plane sapphire. Thin film thickness is ~820 nm. $Mg_xZn_{1-x}O$ and sapphire (*S*) phonon modes are marked by vertical dotted and dashed lines, respectively. The asterisks indicate an additional mode due to Mg in ZnO. The spectra are shifted for clarity.

B. Phonons of *c*-plane hexagonal $Mg_xZn_{1-x}O$ thin films

Figure 3 presents the polarized micro-Raman spectra of a $Mg_{0.23}Zn_{0.77}O$ thin film on *c*-plane sapphire. The spectral features at $\omega=332$, 387, 418, and 438 cm^{-1} can be assigned to a multiphonon (MP) structure, the A_1(TO) mode, the E_1(TO) mode, and the $E_2^{(2)}$ mode, respectively, of the $Mg_{0.23}Zn_{0.77}O$ thin film. In addition to that, spectral features related to the sapphire substrate occur.

Figure 4 shows the Raman spectra in the $x(yy)x'$ scattering geometry of several hexagonal $Mg_xZn_{1-x}O$ thin films. In the $x(yy)x'$ scattering geometry the A_1(TO) mode, the $E_2^{(2)}$ mode, and a MP structure can be studied. With increasing x the A_1(TO) mode shifts to higher frequencies, while the $E_2^{(2)}$ mode and the MP structure do not show a systematic shift and vary only slightly around the values of ZnO (ω[MP]=332 cm^{-1}, $\omega[E_2^{(2)}]$=438 cm^{-1}, Ref. 13). For $x=0.23$, 0.37, and 0.52 an additional mode (AM) around

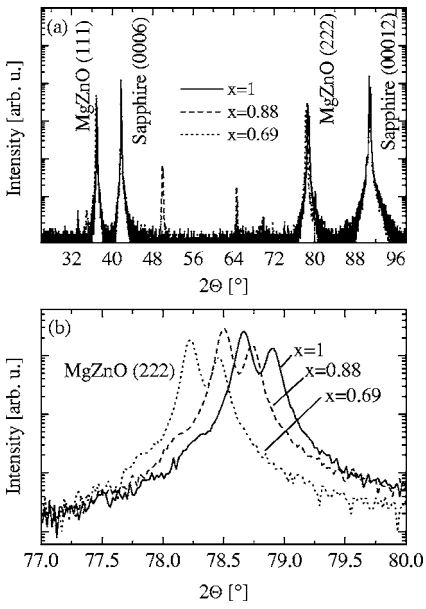

FIG. 2. (a) XRD 2Θ-ω scans of cubic $Mg_xZn_{1-x}O$ thin films with $x=0.69$, 0.88, and 1. (b) Enlargement of the (2 2 2) reflection peak range. The duplet structure of the reflections is caused by the Cu $K\alpha_1$ and Cu $K\alpha_2$ lines of the x-ray diffractometer source.

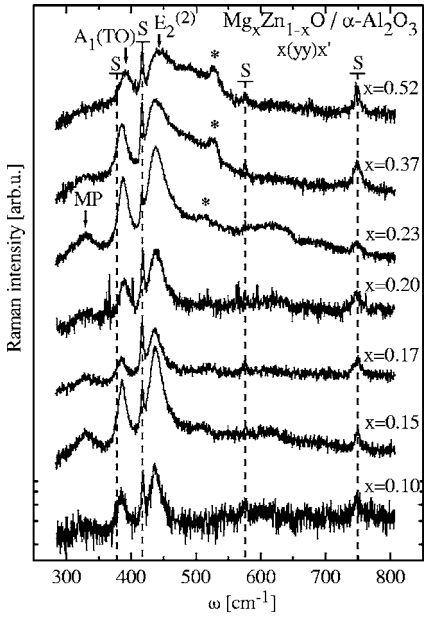

FIG. 4. Micro-Raman spectra in the $x(yy)x'$ scattering geometry of hexagonal $Mg_xZn_{1-x}O$ thin films on *c*-plane sapphire. $Mg_xZn_{1-x}O$ and sapphire (*S*) phonon modes are marked by arrows and vertical dashed lines, respectively. The asterisks indicate an additional mode due to Mg in ZnO. The spectra are shifted for clarity.

TABLE III. Phonon mode frequencies of the $Mg_xZn_{1-x}O$ thin films in Figs. 3 and 4, as determined by Raman scattering.

x	MP (cm^{-1})	A_1(TO) (cm^{-1})	E_1(TO) (cm^{-1})	$E_2^{(2)}$ (cm^{-1})	MM (cm^{-1})
0.52	333	392	~428	440	527
0.37	331	385	~430	438	526
0.23	332	387	418	438	517
0.20	332	388	···	439	···
0.17	331	385	416	437	···
0.15	330	386	417	438	···
0.10	···	385	···	438	···

$\omega \sim 520\ cm^{-1}$ is found. This mode can be assigned to a mixed mode of the $Mg_xZn_{1-x}O$ alloy system, as will be discussed below. Table III summarizes the phonon modes, as determined by Raman scattering, of the hexagonal $Mg_xZn_{1-x}O$ thin films in Figs. 3 and 4.

In Fig. 5 IRSE spectra (Ψ only) of the above examined hexagonal $Mg_xZn_{1-x}O$ thin films on *c* plane sapphire are plotted. The spectral feature at $\omega \sim 600\ cm^{-1}$, which is related to the LO modes, shifts with increasing x to higher frequencies. Further differences compared to the spectra of an undoped ZnO thin film (Ref. 13) occur at $\omega \sim 400\ cm^{-1}$ and $\omega \sim 500\ cm^{-1}$. IRSE analysis revealed two polar lattice modes [$l=2$, $n=0$, Eq. (5)] for polarization $E \perp c$, and one polar lattice and one impurity-type mode [$l=1$, $n=1$, Eq. (5)] for polarization $E \| c$.

Table IV summarizes the phonon mode frequencies, as determined by IRSE, of the hexagonal $Mg_xZn_{1-x}O$ thin films in Fig. 5. The phonon modes of the hexagonal (and cubic) $Mg_xZn_{1-x}O$ thin films versus x are plotted in Fig. 6 for the entire set of samples studied in this work. The A_1(TO) and A_1(LO) branches and the upper branch of the E_1(LO) phonons show an almost linear behavior following the linear interpolation of the corresponding phonon modes of the binary components ZnO and MgO, whereas the lower branch of the E_1(LO) and the two E_1(TO) branches exhibit a nonlinear behavior. In Ref. 18 the modified random element isodisplacement (MREI) model was suggested to describe the phonon mode behavior versus x. A good agreement for the E_1(TO), A_1(TO), and A_1(LO) branches was reported.

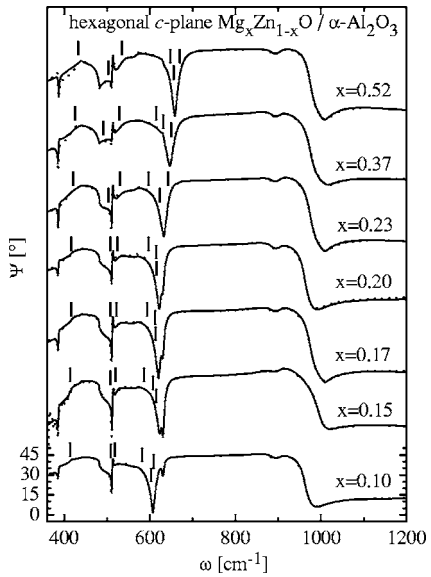

FIG. 5. Experimental (dotted lines) and best-fit model (solid lines) IRSE spectra of hexagonal $Mg_xZn_{1-x}O$ thin films. The spectra are shifted for clarity. The angle of incidence is 55° (samples with $x=0.10, 0.15, 0.17, 0.20$) or 60° (samples with $x=0.23, 0.37, 0.53$). The vertical bars indicate the best-fit phonon mode frequencies, as obtained from IRSE analysis.

The AM of the upper TO branch with E_1 symmetry can be assigned to the mixed mode of the $Mg_xZn_{1-x}O$ alloy, which originates from the local mode Mg in ZnO. The extrapolation to $x=0$ yields an experimental value of $\omega_{loc,ZnO:Mg}=509\ cm^{-1}$. This value agrees well with the calculated local mode $\omega_{loc,1}=518\ cm^{-1}$ in Table II. This confirms the intended substitution of Zn by Mg. The impurity-type mode with A_1 symmetry is tentatively assigned to ordering effects or lattice imperfections.

C. Phonons of *a*-plane hexagonal $Mg_xZn_{1-x}O$ thin films

Figure 7 presents the polarized micro-Raman spectra of an *a*-plane $Mg_{0.075}Zn_{0.925}O$ thin film on *r*-plane sapphire. Because the *c* axes of the *a*-plane $Mg_xZn_{1-x}O$ thin film and of the *r*-plane sapphire substrate are not parallel to each other, the sapphire phonon modes occur in different scattering configurations compared to those of the *c*-plane thin films on *c*-plane sapphire in Fig. 3. For instance, the sapphire phonon

TABLE IV. Best-fit phonon mode frequencies and film thicknesses of the hexagonal $Mg_xZn_{1-x}O$ thin films in Fig. 5, as determined by IRSE. Error bars in parentheses represent the 90% confidence limits.

		$j=\|$		$j=\perp$		$j=\perp$		
x	$\varepsilon_{\infty,j}$[a]	ω_{IM} (cm^{-1})	ω_{LO} (cm^{-1})	$\omega_{TO,1}$ (cm^{-1})	$\omega_{LO,1}$ (cm^{-1})	$\omega_{TO,2}$ (cm^{-1})	$\omega_{LO,2}$ (cm^{-1})	d (nm)
0.52	3.09(0.02)	656 (7)	648 (2)	433.0(0.8)	503 (5)	535 (1)	669.7(1.0)	670 (6)
0.37	3.17(0.01)	615 (1)	632 (1)	425.3(0.4)	491 (5)	529 (1)	649.8(0.7)	1040 (5)
0.23	3.36(0.02)	597 (7)	623 (2)	420.6(0.5)	503 (1)	530 (9)	643.5(1.1)	820 (3)
0.20	3.34(0.03)	597 (1)	615 (1)	415.9(0.5)	508.2(0.9)	524.5(0.7)	615.4(1.0)	960 (2)
0.17	3.40(0.01)	594 (4)	612 (4)	416.1(0.3)	508.1(0.6)	522.3(0.4)	614.2(0.8)	865 (2)
0.15	3.46(0.01)	586.4(0.6)	607.5(0.1)	413.9(0.5)	508.0(0.7)	519.3(0.6)	614.8(0.8)	915 (3)
0.10	3.50(0.01)	581.6(0.6)	602.9(0.1)	413.8(0.3)	509.4(0.5)	518.6(0.4)	608.6(0.7)	860(10)

[a]Assumed to be isotropic ($\varepsilon_{\infty,\|}=\varepsilon_{\infty,\perp}$) during IRSE analysis.

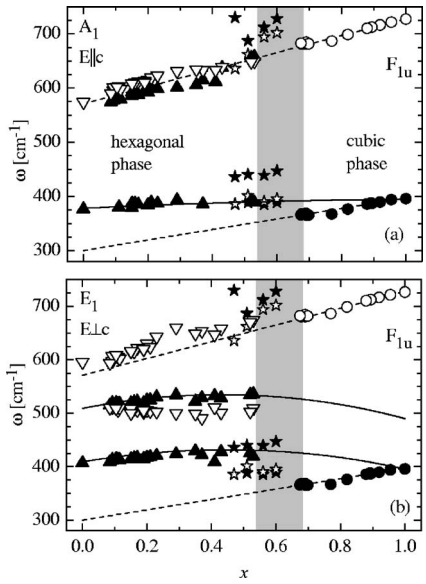

FIG. 6. Phonon mode frequencies of hexagonal $Mg_xZn_{1-x}O$ thin films with A_1 symmetry [panel (a), triangles] and E_1 symmetry [panel (b), triangles], and of cubic $Mg_xZn_{1-x}O$ thin films (circles) with dependence on the Mg mole fraction x. The stars indicate phonon mode frequencies of cubic $Mg_xZn_{1-x}O$ thin films according to Ref. 18. The open and solid symbols represent TO and LO modes, respectively. The dashed lines are linear approximations of the modes of the cubic $Mg_xZn_{1-x}O$ thin films; the solid lines represent MREI calculations for the hexagonal $Mg_xZn_{1-x}O$ thin films redrawn from Ref. 18. The shaded area marks the composition range where the phase transition occurs.

mode at $\omega=645$ cm^{-1} is present in the $x(zz)x'$ and $x(yz)x'$ configurations for the *a*-plane thin film, but only in the $x(zz)x'$ configuration for the *c*-plane thin films.

In Fig. 7 the MP structure at $\omega=333$ cm^{-1}, the A_1(TO) mode at $\omega=381$ cm^{-1}, and the $E_2^{(2)}$ mode at $\omega=440$ cm^{-1} can be identified. Furthermore, a small additional mode at

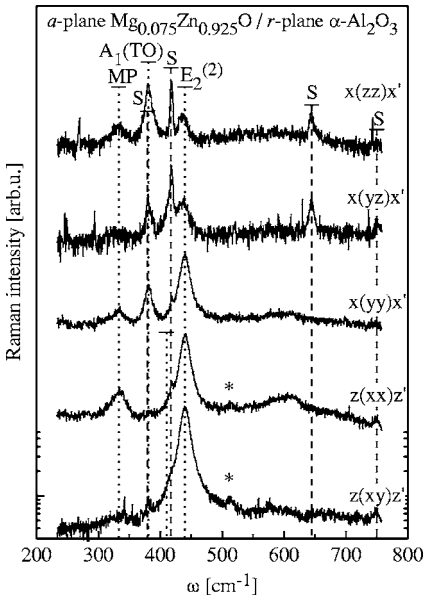

FIG. 7. Polarized micro-Raman spectra of an *a*-plane $Mg_{0.075}Zn_{0.925}O$ thin film on *r*-plane sapphire. Thin film thickness is ~560 nm. $Mg_xZn_{1-x}O$ and sapphire (*S*) phonon modes are marked by vertical dotted and dashed lines, respectively. The asterisks indicate an additional mode. The spectra are shifted for clarity.

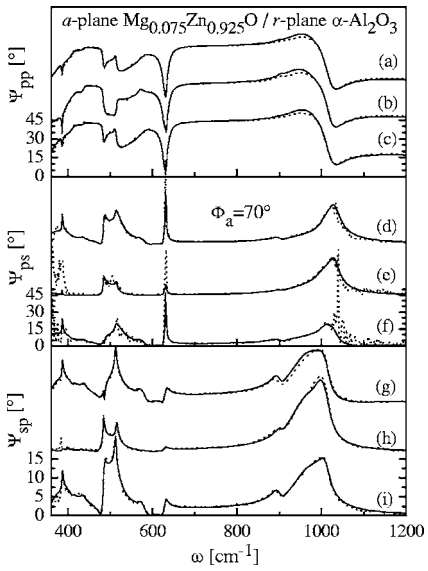

FIG. 8. Experimental (dotted lines) and best-fit model (solid lines) generalized IRSE spectra Ψ_{ij} of an *a*-plane $Mg_{0.075}Zn_{0.925}O$ thin film on *r*-plane sapphire. The panels show from top to bottom the spectra of Ψ_{pp} [spectra (a)–(c)], Ψ_{ps} [(d)–(f)], and Ψ_{sp} [(g)–(i)]. The spectra in (a), (d), and (g) belong to $\varphi_1=-44.4\pm0.5°$; (b), (e), and (h) to $\varphi_2=1.4\pm0.1°$; and (c), (f), and (i) to $\varphi_3=48.7\pm0.4°$, respectively. The angle of incidence is $\Phi_a=70°$. The spectra are shifted for clarity.

512 cm^{-1} can be observed in the $z(xx)z'$ and $z(xy)z'$ scattering configurations. This mode is again assigned to the incorporation of Mg in ZnO.

In Fig. 8 the generalized IRSE spectra (Ψ_{ij} only) of the *a*-plane $Mg_{0.075}Zn_{0.925}O$ thin film are plotted. Data are shown for three different sample orientations and the analysis is carried out as described in Ref. 14 for an *a*-plane ZnO thin film. A point-by-point analysis and a model line shape analysis are performed. In addition to the variation of the dielectric functions, the film thickness of the $Mg_{0.075}Zn_{0.925}O$ thin film and the two sets of Euler angles, which describe the orientation of the *c* axis of the $Mg_{0.075}Zn_{0.925}O$ thin film and the sapphire substrate, respectively, are varied during the analysis procedure.

The best-fit value of the Euler angle θ_{MgZnO} of the $Mg_{0.075}Zn_{0.925}O$ thin film in Fig. 8 is $(91.6\pm0.5)°$, which means that the thin film indeed exhibits an *a*-plane orientation. The best-fit value of the Euler angle $\theta_{sapphire}$ of the sapphire substrate is $(58.9\pm0.5)°$. The nominal value for a perfectly *r*-plane cut sapphire crystal is 57.6°, and our result is in good agreement considering the manufacturing tolerance of ±1°. The Euler angles $\varphi_{MgZnO,i}$ and $\varphi_{sapphire,i}$ are found to be equal within error limits. This is in agreement with previously reported data and our XRD results, from which the epitaxial relation is known to be $[0001]_{MgZnO}\|[0\bar{1}11]_{sapphire}$ and $(11\bar{2}0)_{MgZnO}\|(01\bar{1}2)_{sapphire}$.[19–22] Therefore, we set $\varphi_{MgZnO,i}=\varphi_{sapphire,i}$ for the data analysis procedure.

In Fig. 9 the real and imaginary parts of the DFs ε_j and the imaginary part of the dielectric loss functions $-1/\varepsilon_j$, as obtained by the point-by-point and the model line shape analyses, are plotted. The point-by-point DF for $E\|c$ contains three oscillators at $\omega\sim380$, ~505, and ~575 cm^{-1},

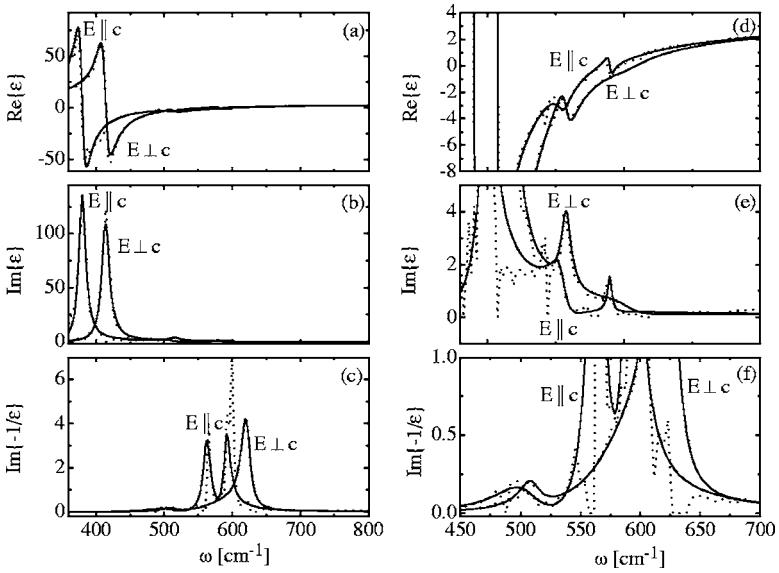

FIG. 9. Real [panels (a) and (d)] and imaginary parts [panels (b) and (e)] of the DFs, and the imaginary part of the dielectric loss functions [panels (c) and (f)] of the $Mg_{0.075}Zn_{0.925}O$ thin film in the reststrahlen region from $\omega=360$ cm^{-1} to $\omega=800$ cm^{-1} [panels (a)–(c)] and in a larger scale from $\omega=450$ cm^{-1} to $\omega=700$ cm^{-1} [panels (d)–(f)]. The dotted lines show the spectra of the point-by-point analysis, while the solid lines show the spectra obtained by the model line shape analysis. The maxima in $\mathrm{Im}(\varepsilon)$ and $-\mathrm{Im}(1/\varepsilon)$ correspond to the TO and LO modes, respectively.

whereas the DF for $E\perp c$ shows at first sight two oscillators at $\omega\sim415$ and ~515 cm^{-1}. The subsequent model line shape analysis revealed a third oscillator for $E\perp c$ at $\omega\sim606$ cm^{-1}, which has a large broadening parameter and, therefore, cannot be seen in the point-by-point fit DF $\varepsilon_\perp$. Table V summarizes the best-fit MDF parameters of sample E342.

The modes with E_1 symmetry at $\omega=515.8$ cm^{-1} and with A_1 symmetry at $\omega=510.3$ cm^{-1} are assigned to the mixed mode, which originates from the local mode of Mg in ZnO, even though the model calculations suggest a higher anisotropy of the local modes (Table II). The origin of the modes with E_1 symmetry at $\omega=579.2$ cm^{-1} and with A_1 symmetry at $\omega=605.3$ cm^{-1} could be ordering effects or lattice imperfections. Further structural investigations are needed for a correct assignment.

In comparison to the results of the c plane $Mg_xZn_{1-x}O$ thin films, the number of detected phonon modes is larger for the a-plane $Mg_xZn_{1-x}O$ thin films. This is very likely due to the limited accessibility of phonon mode parameters when standard IRSE is applied to c-plane oriented, uniaxial thin films.[8] Furthermore, it is possible that the crystal properties of the a-plane $Mg_xZn_{1-x}O$ thin films on r-plane sapphire differ from that of the c-plane $Mg_xZn_{1-x}O$ thin films on c-plane sapphire.

TABLE V. Best-fit IR-MDF ε_∞ and phonon mode parameters of the $Mg_{0.075}Zn_{0.925}O$ thin film shown in Fig. 8. The best-fit thickness is found to be $d=557(3)$ nm. Error bars in parentheses represent the 90% confidence limits.

	ε_∞	$\omega_{TO,1}$	$\omega_{LO,1}$	$\omega_{TO,2}$	$\omega_{LO,2}$	$\omega_{TO,3}$	$\omega_{LO,3}$
		$\gamma_{TO,1}$ (cm^{-1})	$\gamma_{LO,1}$ (cm^{-1})	$\gamma_{TO,2}$ (cm^{-1})	$\gamma_{LO,2}$ (cm^{-1})	$\gamma_{TO,3}$ (cm^{-1})	$\gamma_{LO,3}$ (cm^{-1})
$E\|c$	3.47	379.8	504.7	510.3	563.2	579.2	591.6
	(0.02)	(0.4)	(0.7)	(3.1)	(2.0)	(1.8)	(1.2)
		12[a]	46.5	26.6	13.3	7.1	12[a]
			(1.3)	(0.9)	(1.3)	(0.9)	
$E\perp c$	3.51	414.1	509.0	515.8	588.0	605.6	620.7
	(0.02)	(0.2)	(0.8)	(0.8)	(2.4)	(1.9)	(0.1)
		13.8	20.4	17.7	85.5	70.7	15.4
		(0.5)	(1.5)	(1.6)	(4.3)	(3.9)	(0.1)

[a]Manually adjusted. Not varied during IRSE analysis.

D. Phonons of cubic $Mg_xZn_{1-x}O$ thin films

In accordance with the group theoretical predictions summarized in Sec. II B none of the cubic $Mg_xZn_{1-x}O$ thin films revealed any thin-film-related phonon mode in the Raman spectra. Therefore, only IRSE results are presented here.

Figure 10 shows the IRSE spectra of cubic $Mg_xZn_{1-x}O$ thin films with $x=0.69$, 0.82, 0.88, 0.92, and 1. A very good agreement of the best-fit calculated and experimental data can be seen. IRSE analysis revealed one harmonic oscillator [$l=1$, MDF, Eq. (3)] in the isotropic MDF. Best-fit MDF parameters of the cubic $Mg_xZn_{1-x}O$ thin films in Fig. 10 are summarized in Table VI. A one-mode behavior is found for

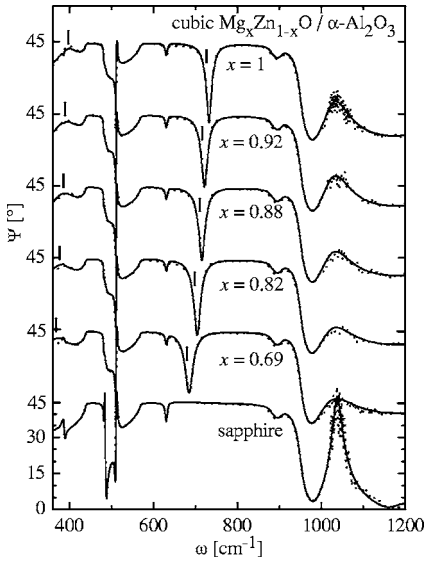

FIG. 10. Experimental (dotted lines) and best-fit calculated (solid lines) IRSE-spectra (Ψ only) of cubic $Mg_xZn_{1-x}O$ thin films on c-plane sapphire and, for comparison, a bare c-plane sapphire substrate. The angle of incidence is 50°. The vertical bars indicate the best-fit phonon mode frequencies, as obtained from IRSE analysis. The spectra are shifted for clarity.

TABLE VI. Best-fit IR-MDF parameters and layer thickness d, as determined by IRSE, for the cubic $Mg_xZn_{1-x}O$ films in Fig. 10. Error bars in parentheses represent the 90% confidence limits.

x	ε_∞	ω_{TO} (cm^{-1})	ω_{LO} (cm^{-1})	γ (cm^{-1})	d (nm)
0.69	3.435	367	680.0	22.9	339
	(0.008)	(2)	(0.1)	(0.3)	(2)
0.82	3.23	376	698.7	19.6)	374
	(0.02)	(2)	(0.2)	(0.2)	(3)
0.88	3.15	387.6	712.0	18.7	344
	(0.02)	(0.7)	(0.1)	(0.2)	(3)
0.92	3.11	389.2	716.3	18.3	323
	(0.02)	(0.7)	(0.1)	(0.2)	(3)
1	3.06	395.6	727.0	16.0	325
	(0.01)	(0.5)	(0.1)	(0.2)	(2)

the phonon mode frequencies. As predicted by the model calculations in Sec. II E no additional mode, which originates from a local mode of Zn in MgO, is observed. The phonon mode frequencies of the cubic MgO thin film agree well with values of MgO single crystals (ω_{TO}=401 cm^{-1}, ω_{LO}=719 cm^{-1}, Ref. 40). Phonon mode frequencies versus x are plotted in Fig. 6. An almost linear shift for both ω_{TO} and ω_{LO} with x can be seen. The shift of the TO and LO modes can be modeled by a linear composition dependence $\omega_{TO;LO}(x)=m_{TO;LO}x+n_{TO;LO}$ with best-fit coefficients m_{TO}=97(4) cm^{-1}, n_{TO}=300(3) cm^{-1}, m_{LO}=157(10) cm^{-1}, and n_{LO}=571(9) cm^{-1}.[17] The extrapolation to x=0 yielded a value of $\omega_{TO}(0)\sim 300$ cm^{-1} and $\omega_{LO}(0)\sim 570$ cm^{-1}, which should address ω_{TO} and ω_{LO}, respectively, of cubic ZnO. No experimental data have been reported for cubic ZnO at normal ambient conditions yet. In Ref. 41 *ab initio* calculations for phonon properties of cubic ZnO were presented, which used the experimental data of rocksalt-structure ZnO studied at high pressures (~8 GPa) as input parameters. According to these calculations ω_{TO} and ω_{LO} of cubic ZnO were predicted to be 235 and 528cm^{-1}, respectively. The values are smaller than those obtained from the IRSE analysis described above, but both extrapolations follow the same trend in predicting phonon mode frequencies, which are smaller than those of hexagonal ZnO. This behavior is assigned to the change of coordination.

Figure 6 contains also previously published data of cubic $Mg_xZn_{1-x}O$ thin films with $0.47\leqslant x\leqslant 0.6$ deposited by low temperature (250 °C) REBE on c-plane sapphire.[18] The phonon mode frequencies in Ref. 18 are determined by reflectivity measurements and show a considerable difference from the data of the cubic $Mg_xZn_{1-x}O$ thin films studied by this group. The data in Ref. 18 would fit surprisingly well to the data of our hexagonal $Mg_xZn_{1-x}O$ thin films. Discrepancies in the results of this work and Ref. 18 indicate a complex transition region behavior for $Mg_xZn_{1-x}O$ between the wurtzite and rocksalt structure. It is likely that the existence of a single- or double-phase material will depend on composition, growth parameters, and growth technique.

In Fig. 11 the best-fit phonon mode broadening parameters γ of the cubic $Mg_xZn_{1-x}O$ thin films are plotted versus x. γ decreases almost linearly with increasing x, which reflects an alloy-induced disorder. Only the $Mg_xZn_{1-x}O$ thin film with x=0.78 does not follow the linear composition dependence. The $Mg_{0.78}Zn_{0.22}O$ thin film was grown at a higher partial oxygen pressure [$p(O_2)$=0.16 mbar] than all the other cubic $Mg_xZn_{1-x}O$ thin films [$p(O_2)$=0.01, ..., 0.053 mbar]. Therefore, γ is not only increased by the alloy-induced effect, but also by a lower crystal quality. Similar effects of a lower crystal quality on the phonon mode broadening parameters were reported in Ref. 42 for ZnO thin films on silicon. The lower crystal quality of the $Mg_{0.78}Zn_{0.22}O$ thin film is confirmed by XRD results.

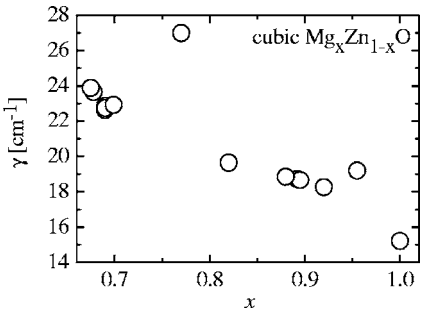

FIG. 11. Best-fit phonon mode broadening parameters, as obtained by IRSE, of the cubic $Mg_xZn_{1-x}O$ thin films.

E. Dielectric constant parameters

Figure 12 summarizes high-frequency and static dielectric constants of our PLD-grown $Mg_xZn_{1-x}O$ thin films. The high-frequency dielectric constants are determined by IRSE, whereas the static dielectric constants are calculated from the

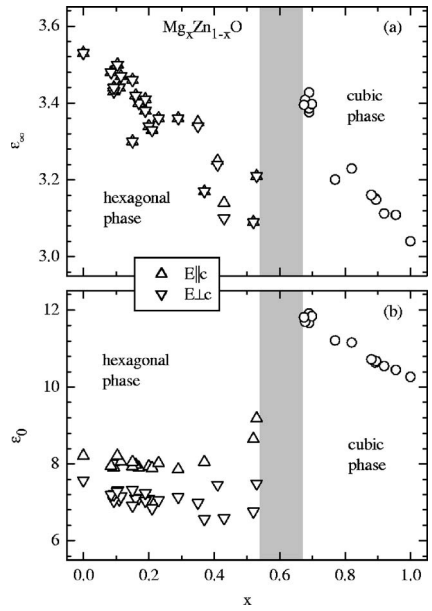

FIG. 12. High-frequency dielectric constants (a) and static dielectric constants (b) of hexagonal ($E\|c$: upright triangles, $E\perp c$: downright triangles) and cubic (circles) $Mg_xZn_{1-x}O$ thin films. The shaded area indicates the composition range of the phase transition.

high-frequency dielectric constants and the phonon mode frequencies in Fig. 6 using the Lydanne-Sachs-Teller relation [Eq. (4)].

Besides the natural disappearance of the anisotropy both high-frequency and static dielectric constants change abruptly upon phase transition from wurtzite to rocksalt structure due to the coordination number change (fourfold to sixfold) and the associated change of bond polarizability (increase in splitting between TO- and LO-mode frequencies, Fig. 6), and critical-point characteristics of the two polytypes.

An abrupt change of the dielectric constants should affect electronic properties, for instance, the exciton binding energy E_{ex}^{b}. The following equation is known from semiconductor textbooks:[43]

$$E_{\mathrm{ex}}^{b} = 13.6\ \mathrm{eV}\frac{\mu_{\mathrm{ex}}}{m_0}\frac{1}{n_B^2\varepsilon_0^2}. \tag{15}$$

μ_{ex}, m_0, and n_B are the reduced exciton mass, the electron rest mass, and the principal quantum number ($n_B = 1,2,3,\ldots$), respectively. μ_{ex} is defined by

$$\mu_{\mathrm{ex}} = \frac{m_e^* m_h^*}{m_e^* + m_h^*}m_0, \tag{16}$$

where m_e^* and m_h^* are the effective electron and hole masses, respectively. From spectroscopic ellipsometry studies in the band-gap spectral region, it is known that the change of the exciton binding energy of our $Mg_xZn_{1-x}O$ thin films upon phase transition is negligible.[5,6,44–46] Because the static dielectric constant changes abruptly upon phase transition, the reduced exciton mass must change too. Our ε_0 data suggest that μ_{ex} must increase by a factor of about 2 when the crystal structure changes from wurtzite to rocksalt. In Ref. 43 it was pointed out that Eq. (15) holds only if E_{ex}^{b} is small compared to the optical phonon energy $\hbar\omega_{\mathrm{LO}}$. For ZnO and MgO, E_{ex}^{b} (ZnO: 60 meV, MgO: 85 meV) is similar to $\hbar\omega_{\mathrm{LO}}$ (ZnO: 70 meV, MgO: 90 meV). Consequently, corrections to Eq. (15) have to be made. For instance, the Haken potential approach suggests replacing ε_0 by a value which interpolates between ε_0 and ε_∞ depending on the distance between electron and hole.[43] Parameters which are necessary for the calculation of this correction are unknown. Therefore, further quantitative considerations are not possible. However, both ε_0 and ε_∞ increase upon phase transition from wurtzite to rocksalt crystal structure. Therefore, the interpolated value between ε_0 and ε_∞ should increase too upon phase transition if the distance between electron and hole is assumed to be similar for both crystal phases. Hence, independent of the consideration of ε_∞, ε_0, or an interpolated value between both, μ_{ex} must increase upon phase transition from wurtzite to rocksalt crystal structure. The factor of increment is limited by the maximal change of ε_0^2, which is about 2. If μ_{ex} changes, the effective mass parameters must change too. No experimental and theoretical data for effective mass parameters of $Mg_xZn_{1-x}O$ are available so far. Therefore, no predictions concerning the change of the effective mass parameters upon phase transition can be made here.

ε_∞ of the cubic $Mg_xZn_{1-x}O$ thin films decreases almost linearly with increasing x. The best-fit linear approximation $\varepsilon_\infty = A + B\cdot x$ is obtained with parameters $A = (4.145 \pm 0.029)$ and $B = (-1.107 \pm 0.032)$. This suggests a value of 4.145 for ε_∞ of cubic ZnO, which is larger than the values obtained for hexagonal ZnO thin films ($\varepsilon_\infty = 3.6, \ldots, 3.76$, Refs. 4, 13, and 14). In Ref. 41 a value of 5.44 for ε_∞ of rocksalt ZnO was predicted from first-principles calculations.

V. SUMMARY

Infrared spectroscopic ellipsometry and Raman scattering are applied to study the long-wavelength optical phonon modes and dielectric constants of PLD-grown, hexagonal and cubic $Mg_xZn_{1-x}O$ thin films on sapphire in the composition range $0 \leqslant x \leqslant 1$. For the cubic $Mg_xZn_{1-x}O$ thin films with $x \geqslant 0.67$, a one-mode behavior is found, where the TO and LO modes and dielectric constants shift linearly with x. The hexagonal c-plane oriented $Mg_xZn_{1-x}O$ thin films with $x \leqslant 0.53$ show two modes for each polarization $E \perp c$ and $E \| c$. Generalized ellipsometry is applied to a-plane $Mg_xZn_{1-x}O$ thin films, which allows accessing the full dielectric tensor parameters. Here three phonon modes for each polarization $E \perp c$ and $E \| c$ are detected. Phonon mode polarizability and dielectric constants change abruptly upon phase transition from wurtzite (fourfold coordinated) to cubic rocksalt (sixfold coordinated) crystal structure. Consequently, an increase of the reduced exciton mass and effective electron mass upon phase transition up to a factor of 2 is proposed. All changes are assigned to the change of coordination.

ACKNOWLEDGMENTS

This work was supported by the Deutsche Forschungsgemeinschaft (DFG) under Grant No. SCHUH1338/3-1, and within the DFG research units 404 (Gr 1011/14-1, SCHUH1338/4-1, and SCHUH1338/4-2) and 522 (Gr 1011/11-1). The authors acknowledge D. Speeman for RBS measurements. They also thank the technical help of U. Teschner (Raman), H. Hochmuth (PLD), E. M. Kaidashev (PLD), and G. Ramm (PLD).

[1] W. Hirschwald *et al.*, *Current Topics in Materials Science* (North-Holland, Amsterdam, 1981), Vol. 7.
[2] D. M. Roessler and W. C. Walker, Phys. Rev. Lett. **17**, 310 (1966).
[3] A. Ohtomo *et al.*, Appl. Phys. Lett. **72**, 2466 (1998).
[4] C. W. Teng, J. F. Muth, Ü. Özgür, M. J. Bergmann, H. O. Everitt, A. K. Sharma, C. Jin, and J. Narayan, Appl. Phys. Lett. **76**, 979 (2000).
[5] R. Schmidt *et al.*, Appl. Phys. Lett. **82**, 2260 (2003).
[6] R. Schmidt *et al.*, *Proceedings of the 26th International Conference on The Physics of Semiconductors*, Institute of Physics Conference Series Vol. **171**, edited by A. R. Long and J. H. Davis (IOP, Bristol, 2003), p. 11.
[7] MRS News, MRS Bull. **28**, 314 (2003).
[8] M. Schubert, *Infrared Ellipsometry on Semiconductor Layer Structures: Phonons, Plasmons, and Polaritons* (Springer, Berlin, 2004).
[9] M. Schubert *et al.*, Phys. Status Solidi A **228**, 437 (2001).
[10] M. Schubert, T. Hofmann, and C. M. Herzinger, J. Opt. Soc. Am. A **20**, 347 (2003).
[11] A. Kasic, M. Schubert, S. Einfeldt, and D. Hommel, Vib. Spectrosc. **29**, 121 (2002).
[12] A. Kasic *et al.*, Phys. Status Solidi C **0**, 1750 (2003).
[13] N. Ashkenov *et al.*, J. Appl. Phys. **93**, 126 (2003).
[14] C. Bundesmann, N. Ashkenov, M. Schubert, A. Rahm, H. v. Wenckstern, E. M. Kaidashev, M. Lorenz, and M. Grundmann, Thin Solid Films **455&456**, 161 (2003).

[15]C. Bundesmann *et al.*, Appl. Phys. Lett. **81**, 2376 (2002).
[16]C. Bundesmann, M. Schubert, D. Spemann, A. Rahm, H. Hochmuth, M. Lorenz, and M. Grundmann, Appl. Phys. Lett. **85**, 905 (2004).
[17]C. Bundesmann, Ph.D. thesis, Universität Leipzig, 2005 (Shaker, Aachen, 2006).
[18]J. Chen and W. Z. Shen, Appl. Phys. Lett. **83**, 2154 (2003).
[19]M. Wraback, H. Shen, S. Liang, C. R. Gorla, and Y. Lu, Appl. Phys. Lett. **74**, 507 (1999).
[20]C. R. Gorla, N. W. Emanetoglu, S. Liang, W. E. Mayo, Y. Lu, M. Wraback, and H. Shen, J. Appl. Phys. **85**, 2595 (1999).
[21]S. Muthukumar, J. Zhong, Y. Chen, Y. Lu, and T. Siegrist, Appl. Phys. Lett. **82**, 742 (2003).
[22]B. P. Zhang, Y. Segawa, K. Wakatsuki, Y. Kashiwaba, and K. Haga, Appl. Phys. Lett. **79**, 3953 (2001).
[23]T. C. Damen, S. P. S. Porto, and B. Tell, Phys. Rev. **142**, 570 (1966).
[24]*The Raman Effect, Vol. 2: Applications*, edited by A. Anderson (Dekker, New York, 1973).
[25]R. H. Lyddane, R. G. Sachs, and E. Teller, Phys. Rev. **59**, 673 (1941).
[26]A. Kasic, M. Schubert, S. Einfeldt, D. Hommel, and T. E. Tiwald, Phys. Rev. B **62**, 7365 (2000).
[27]T. Hofmann, G. Leibiger, I. Pietzonka, V. Gottschalch, and M. Schubert, Phys. Rev. B **64**, 155206 (2001).
[28]R. M. A. Azzam and N. M. Bashara, *Ellipsometry and Polarized Light* (North-Holland, Amsterdam, 1977).
[29]*Handbook of Ellipsometry*, edited by H. G. Tompkins and E. A. Irene (William Andrews, Norwich, NY, 2005).
[30]M. Schubert, in *Handbook of Ellipsometry*, edited by H. G. Tompkins and E. A. Irene (William Andrews, Norwich, NY, 2005), Chap. 9, p. 875 et seqq.
[31]A. S. Barker and A. J. Sievers, Rev. Mod. Phys. **47**, S1 (1975).
[32]G. Lucovsky, M. H. Brodsky, and E. Burstein, Phys. Rev. B **2**, 3295 (1970).
[33]M. Mazur, E. W. Montroll, and R. B. Potts, J. Wash. Acad. Sci. **46**, 2 (1956).
[34]M. Lorenz *et al.*, Solid-State Electron. **43**, 2205 (2003).
[35]D. Spemann, E. M. Kaidashev, M. Lorenz, J. Vogt, and T. Butz, Nucl. Instrum. Methods Phys. Res. B **219&220**, 891 (2004).
[36]M. Schubert, T. E. Tiwald, and C. M. Herzinger, Phys. Rev. B **61**, 8187 (2000).
[37]S. Choopun, R. D. Vispute, W. Yang, R. P. Sharma, T. Venkatesan, and H. Shen, Appl. Phys. Lett. **80**, 1529 (2002).
[38]J. Chen, W. Z. Shen, N. B. Chen, D. J. Qiu, and H. Z. Wu, J. Phys.: Condens. Matter **15**, L475 (2003).
[39]M. Sanati, G. L. Hart, and A. Zunger, Phys. Rev. B **68**, 155210 (2003).
[40]J. R. Jasperse, A. Kahan, J. N. Plendl, and S. S. Mitra, Phys. Rev. **146**, 526 (1966).
[41]J. Serrano, A. H. Romero, F. J. Manjón, R. Lauck, M. Cardona, and A. Rubio, Phys. Rev. B **69**, 094306 (2004).
[42]S. Heitsch *et al.*, Thin Solid Films **496**, 234 (2005).
[43]C. F. Klingshirn, *Semiconductor Optics* (Springer, Berlin, 1997).
[44]R. Schmidt-Grund *et al.*, Thin Solid Films **455&456**, 500 (2004).
[45]R. Schmidt-Grund *et al.*, AIP Conf. Proc. **772**, 201 (2005).
[46]R. Schmidt-Grund *et al.*, J. Appl. Phys. (to be published).